CO Oxidation at SnO2/Pt3Sn(111) Interfaces

Topics in Catalysis (2018) 61:1458–1464
https://doi.org/10.1007/s11244-018-1044-9

ORIGINAL PAPER

CO Oxidation at $SnO_2/Pt_3Sn(111)$ Interfaces

Matthias Vandichel[1] · **Henrik Grönbeck**[1]

Published online: 1 September 2018

Abstract
Segregation induced formation of oxide/metal interfaces can significantly influence the catalytic activity of alloy nanoparticles. One example is Pt_3Sn nanoparticles, which are known to segregate into SnO_X and an Sn deficient alloy phase during typical operating conditions for CO oxidation. Here, we use density functional theory calculations to investigate CO oxidation over $Pt_3Sn(111)$ supported SnO_2 and $(SnO_2)_3$, representing the initial state of segregation. The results are compared to CO oxidation at an interface between bulk-like SnO_2 and $Pt_3Sn(111)$. The barrier for CO oxidation via a Mars–van Krevelen mechanism is found to be lower on SnO_2 and $(SnO_2)_3$ as compared to the bulk-like model. However, the regeneration of the finite systems is associated with higher barriers for O_2 dissociation which may become the rate limiting step in the low temperature regime where the metal surface can be assumed to be CO covered.

Graphical Abstract

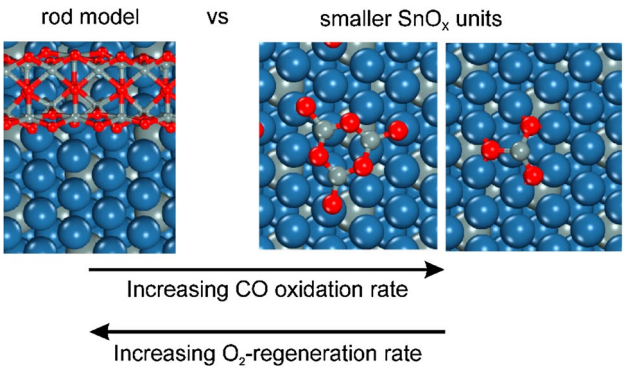

Keywords Bimetallic catalysts · CO oxidation · Heterogeneous catalysis · Metal oxides

1 Introduction

Bimetallic alloys represent an important class of catalysts in heterogeneous catalysis where PtSn is one example that has been investigated for low-temperature CO oxidation [1–4]. The effects of alloying on catalytic properties are generally described in terms of ensemble, ligand and strain effects [5–8]. Ensemble effects refer to geometric adsorption constraints upon alloying, whereas ligand and strain effects denote changes in the electronic structure. The mixing pattern in metal nanoalloys is generally complex and depends both on the constituent metals and the synthesis method [9–11]. Nanoalloys have been investigated extensively

Electronic supplementary material The online version of this article (https://doi.org/10.1007/s11244-018-1044-9) contains supplementary material, which is available to authorized users.

✉ Matthias Vandichel
matvan@chalmers.se

[1] Department of Physics and Competence Centre for Catalysis, Chalmers University of Technology, 412 96 Gothenburg, Sweden

computationally [9], and recent efforts include examples where the chemical ordering of bimetallic nanoparticles is predicted on the basis of density functional theory (DFT) calculations [12]. Although this approach is suited to explore the homotop distribution for PtSn bimetallic nanoparticles of particular shape and composition [13], it does not describe adsorbate (or reaction) induced segregation phenomena.

The dynamic response of metal nanoparticles to adsorbates makes it challenging to assess the origin of promoting effects upon alloying. Several studies have demonstrated that reactions may drive surface reconstruction and/or segregation [14–16]. Also in the case of PtSn nanoparticles, experimental evidence exists for adsorbate induced segregation during typical operating conditions for regular CO-oxidation and preferential CO-oxidation in the presence of H_2 (PROX) [2–4]. In Ref. [3], ambient pressure X-ray photoelectron spectroscopy (XPS) showed the formation of an Sn-oxide phase during CO-oxidation over silica supported PtSn nanoparticles. Based on the experiments, [3] it was suggested that CO oxidation occurs with a low activation barrier at the interface between Pt and SnO_x domains via a Mars–Van Krevelen mechanism [17]. Moreover, SnO_2-phases in contact with a PtSn nanoalloy have been observed during CO electro-oxidation over PtSn with transmission electron microscopy [18]. Furthermore, Pt-Sn segregation during CO exposure over alumina supported PtSn has been inferred from in situ diffuse reflectance IR Fourier transform spectroscopy following the CO stretch vibration [1, 2, 4]. In the case of Pt_3Sn, adsorbate induced segregation is not limited to nanoparticles and it has been observed for $Pt_3Sn(111)$ during CO oxidation with X-ray photoemission spectroscopy (XPS) [19]. In particular, it was proposed that $Pt_3Sn(111)$ converts to an inverse catalyst with SnO_X supported by metallic Pt_3Sn [19].

Adsorbate induced segregation of bi-metallic nanoparticles leads to the creation of interfaces and during oxidation reactions, metaloxide/metal interfaces or metaloxide/metaloxide interfaces are formed. It is well known, that such interfaces can have superior catalytic performance in CO oxidation [20–26]. For example, low temperature activity has been observed for promoted Pt-group metals [23] and in the case of $FeO_x/Pt(111)$, the activity was rationalized by the possibility to have CO oxidation at the FeO_x/Pt interface [20]. In case of Pt_3Sn, segregation into an SnO_2 phase supported by a $Pt(111)/Pt_3Sn$ (Pt-skin) was recently computationally predicted via ab initio thermodynamics [24]. Moreover, the importance of an oxide/metal interface for the reaction kinetics was explored using first principle micro-kinetic modeling for a periodic SnO_2-rod supported by a Pt-skin [24]. The catalytic role of the SnO_X-phase was manifested by a low temperature activity at the interface. The reaction path at the interface is of Mars–van Krevelen type which limits the effect of CO poisoning that controls the low temperature reaction rate on regular Pt, where the reaction proceeds via a Langmuir–Hinshelwood mechanism. Furthermore, the CO-oxidation barriers at the SnO_X/Pt interface were found to be lower than the corresponding barrier on the metal-only system. As it is difficult to know the experimental degree of segregation, especially during the initial stages, it is unknown whether the results for the bulk-like SnO_2 interface can be generalized to other SnO_x-structures supported on Pt. Therefore, it is desirable to investigate how CO oxidation barriers and their regeneration with O_2 depend on the size of the SnO_X-phase.

Herein, we use DFT calculations to investigate CO oxidation and O_2 regeneration over finite size SnO_2 and $(SnO_2)_3$ units supported on $Pt_3Sn(111)$. The results are compared to oxidation at a bulk-like metal supported SnO_2-phase, represented by a SnO_2-rod/$Pt_3Sn(111)$ model.

2 Theoretical Methodology

DFT is applied with the gradient corrected exchange-correlation functional according to Perdew, Burke and Ernzerhof [27]. In particular, the Vienna Ab Initio Simulation Package [28, 29] is used. The one-electron Kohn–Sham orbitals are expanded in a plane-wave basis-set with a kinetic energy cutoff of 450 eV. PAW potentials are employed to describe the interaction between the valence electrons and the core [30]. Reciprocal space integration over the Brillouin zone is approximated with finite sampling using Monkhorst–Pack grids [31, 32]. Bulk calculations of Pt, Pt_3Sn, SnO_2 are performed with a k-point grid of at least $12\times12\times12$. Surface calculations are performed using 5 layered orthorhombic slabs. $(4\times2\sqrt{3})_{rect}$ or $p(4\times4)$ surface cells are used for the metal-only surfaces and the metal-supported SnO_2 and $(SnO_2)_3$ units. A $(6\times2\sqrt{3})_{rect}$ surface cell is used to model a metal-supported periodic $(SnO_2)_{12}$-rod. k-point grids are employed depending on the size of the surface cell being either $3\times3\times1$ or $2\times3\times1$. A vacuum layer of at least 20 Å is used in the calculations.

The systems are structurally optimized until the largest force is smaller than 0.03 eV/Å. Transition states are obtained initially with the climbing image nudged elastic band method [33, 34] and further refined with the dimer method [35]. The convergence criteria for the transition state searches are set to at least 0.03 eV/Å. For the O_2 dissociation reactions, spin polarized calculations are employed for both reactants and transition states. To verify transition states and local minima, a partial Hessian vibrational analysis (PHVA) is employed. The PHVA is performed only for the surface species while keeping the rest of the system fixed. The numerical partial Hessian is calculated by displacements in x, y and z-directions of ±0.02 Å.

The stability of the segregated systems of the form $(SnO_2)_X$ is assessed by referencing to SnO_2-bulk. The stability (ΔE) is calculated according to:

$$\Delta E = E_{(SnO_2)_x/Pt(111)/Pt_3Sn} - xE_{SnO_2,\ bulk} - E_{Pt(111)/Pt_3Sn}$$

Here, $E_{(SnO_2)_x/Pt(111)/Pt_3Sn}$ is the energy of the system under consideration, $E_{SnO_2,\ bulk}$ is the energy of the SnO_2-bulk and $E_{Pt(111)/Pt_3Sn}$ is the energy of a Pt_3Sn slab with the top layer being only Pt (a Pt-skin).

3 Results and Discussion

The reaction induced segregation process is complex on Pt_3Sn–nanoparticles. From experiments, it is clear that SnO_X is formed during CO oxidation, [3, 19] however, the morphology is unknown. Here, we present first different SnO_2/Pt interface models and their relative stability with respect to bulk SnO_2 (Sect. 3.1). Thereafter, CO adsorption, the stability of the interface O atoms and CO oxidation are investigated (Sect. 3.2). The closing of the catalytic cycle by regeneration of SnO_X via O_2 dissociation is investigated in Sect. 3.3.

3.1 Interface Models and Their Relative Stability

Different SnO_X model structures are constructed on a Pt-skin model, thus a $Pt_3Sn(111)$ slab with the top-most metal layer being Pt-only. A Pt-skin is used instead of regular $Pt_3Sn(111)$ to model the Sn-deficiency in the alloy. This model system was previously used to explore CO oxidation routes on PtSn nanoparticles [24]. The studied interface models studied herein are displayed in Fig. 1. ROD represents a $(SnO_2)_{12}$-rod, with exposed $SnO_2(110)$-surfaces as the (110) facet is known to be the stable SnO_2 surface [36, 37]. The TRIMER system is a trimeric $(Sn_3O_3)O_3$ structure and the MONOMER unit is a single Sn ad-atom with two oxygen atoms. For each of the models, a favorable orientation was obtained by optimizing a set of different generated structures. Here, only the lowest energy orientation is considered for further studies.

In earlier work, the exothermicity of segregation was validated for the formation of the rod model onto a five layer Pt_3Sn slab in absence of CO [24]. It was found that the required oxygen chemical potential for segregation of this slab into an Sn-deficient Pt-skin system and bulk SnO_2 is − 1.53 eV. If instead of bulk SnO_2 a rod-model is formed (Fig. 1a), an oxygen chemical potential of − 1.17 eV is required. With respect to bulk SnO_2, the stabilities (ΔE) are 0.72 eV (rod), 1.24 eV (trimer) and 1.44 eV (monomer) (see Fig. 1). From the stability difference, the minimum oxygen chemical potential to form the $(SnO_2)_3$ and (SnO_2) is calculated to be − 0.91 eV and − 0.81 eV, respectively. In the

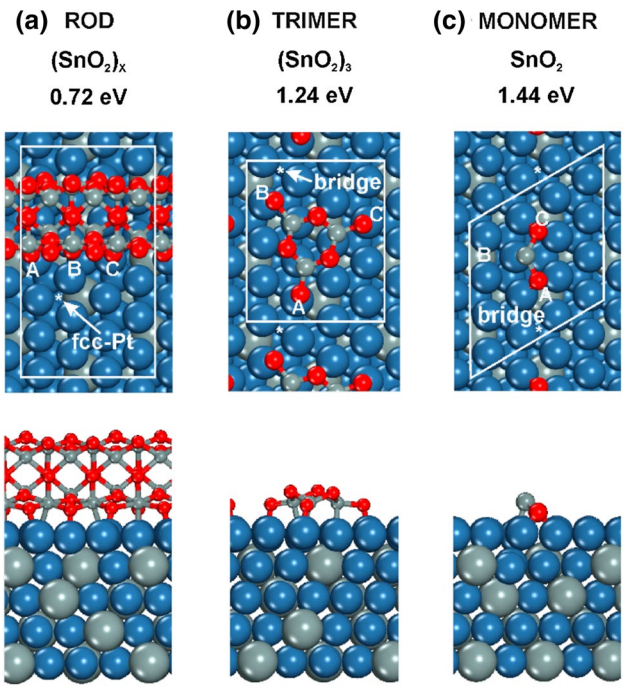

Fig. 1 Structural models of the considered $(SnO_2)_X$ phases supported on a Pt-skin system; **a** periodic $(SnO_2)_{12}$ rod model in a $(6 \times 2\sqrt{3})_{rect}$ surface cell, **b** trimeric $(SnO_2)_3$ unit in a $(4 \times 2\sqrt{3})_{rect}$ surface cell and **c** a SnO_2 monomer in a p(4×4) surface cell. The surface cells are indicated by white lines. The stability (ΔE) of the $(SnO_2)_X$ phases with respect to bulk SnO_2 is indicated. An asterisk (*) denotes the considered position for CO adsorption. Atomic color codes: O (red), Sn (gray) and Pt (blue)

presence of CO and O_2, the formation of monomeric and trimeric SnO_2 units should precede the formation of more bulk like SnO_2-phases, such as the rod model. However, due to the lower stability of the monomer and the trimer, their formation requires higher oxygen chemical potentials and, thus, higher oxygen pressures than the formation of the rod. The minimal oxygen pressure needed to form monomers at a temperature of 400 K is still very low, being ~ 10^{-11} bar [24]. The corresponding pressures for the trimer and the rod are about 10^{-13} and 10^{-19} bar, respectively.

3.2 Relative Stability of Interface Oxygens, CO Adsorption and CO Oxidation at SnO_X Interfaces

The model systems have, completely oxygen saturated, three or two oxygen atoms available for reaction, see Fig. 1. A measure of their reactivity is given by the stability which could be assessed by calculating the energy required to form oxygen vacancies. The vacancy formation energies, defined as the energy needed to form 1/2 O_2 in the gas phase, are given in Table 1. For rod and trimer models, the oxygen with the lowest vacancy formation energy is denoted position in B. Owing to symmetry, the two atoms (A and C) are

Table 1 Oxygen vacancy formation energies and reaction barriers for the considered systems

	Rod $(SnO_2)_X$/Pt-skin	Trimer $(SnO_2)_3$/Pt-skin	Monomer (SnO_2)/Pt-skin
$E_{ads,O-A}$	−1.30‡	−1.11	−0.59[a]
$E_{ads,O-B}$	−1.24‡	−0.61	–
$E_{ads,O-C}$	−1.30‡	−0.92	−0.59[a]
$E_{ads,CO\ near\ O-B}$	−1.99‡ (fcc-Pt)	−1.70 (bridge)	−1.88 (bridge)
$\Delta E^{‡,int}$	0.91‡	0.29	0.63
$\Delta E^{‡,CO/Pt-skin}$	1.01‡	0.67	0.83

The reaction barrier $\Delta E^{‡}$ is calculated with respect to CO adsorbed in an fcc-Pt position in a $(4 \times 2\sqrt{3})_{rect}$ unit cell, thus in the absence of repulsive interactions with the SnO_x-phase. The positions for the oxygen atoms in the rod are labeled according to Fig. 1. The energies are reported in eV without zero-point corrections

‡From Ref. [24]

[a]For monomer, the A and C positions are equivalent

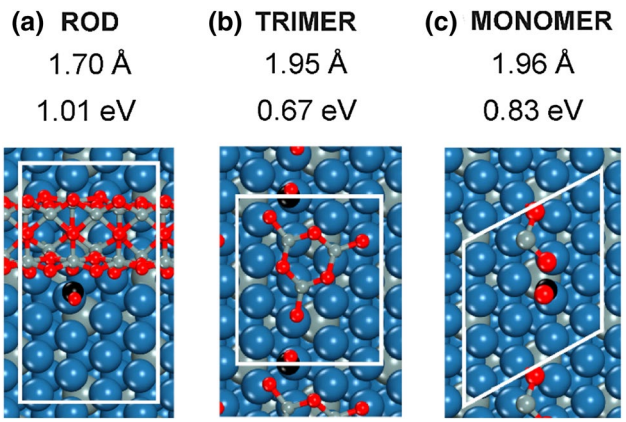

Fig. 2 Structural models of the CO oxidation transition states. The C–O distance of the forming bond is given together with barrier with respect to a common CO reference state at the Pt-skin. Atomic color codes: C (black), O (red), Sn (gray) and Pt (blue)

equivalent for the monomer. The vacancy formation energies to go from state ABC to A*C are 1.24 and 0.61 eV, for the rod and the trimer, respectively. For the monomer, the vacancy formation energy going from A*C to **C is 0.59 eV. The vacancy formation energies on the trimer and monomer models are, thus, considerably lower than on the rod model. In case of the trimer, vacancy formation from A or C atoms requires more energy than from B, whereas the differences are moderate for the rod.

CO oxidation is one possibility to deplete oxygen atoms by reactions from the SnO_X systems. Here, we assume the consumption of the oxygen atom in position B via CO oxidation forming A*C for rod and trimer models and consumption of position A for the monomer model forming **C. CO can adsorb on a multitude of positions on the Pt-skin. In particular, there are different types of sites with respect to the underlying Pt_3Sn lattice. The different types of hollow sites (fcc-Pt, fcc-Sn, hcp-Pt and hcp-Sn) are visualized in Fig. S1 of the Electronic Supplementary Material (ESM). For example, fcc-Pt refers to a site where a Pt atom is situated in the third layer below the site, for fcc-Sn an Sn atom appears in the third layer. The CO adsorption energies are −1.99 eV (fcc-Pt, rod), −1.70 eV (bridge, trimer) and −1.88 eV (bridge, monomer). The CO adsorption energies near the trimer and the monomer deviate markedly from the adsorption energy of CO on a $(4 \times 2\sqrt{3})_{rect}$ Pt-skin system, being −2.09 eV in the fcc-Pt position which is related to repulsive CO–SnO_x interactions.

Barriers for all model systems are evaluated with respect to CO adsorbed in an fcc-Pt or bridge position near the consumed oxygen (see * in Fig. 1). The CO oxidation barriers from the $(SnO_2)_X$-state [ABC→A*C for rod and trimer, and A*C→**C for monomer] are 0.91 eV, 0.29 eV and 0.63 eV for the rod, trimer and monomer, respectively. If instead the same reference state for CO is used, being CO on the Pt-skin far from the metal oxide phase in an fcc-Pt position, the barriers are 1.01 eV (rod), 0.67 eV (trimer) and 0.83 eV (monomer), see Table 1. The CO oxidation barriers on the smaller SnO_X models are, thus, considerably lower than for the rod-model. This is evident also in the large variation of the O–CO transition state structures, see Fig. 2. From the A*C configuration, the subsequently consumed oxygen is chosen to be A for the rod and trimer models. While the barrier for (A*C→**C), is about 0.20 eV higher than ABC→B*C, for the rod, the increase is within 0.10 eV for the trimer (see Fig. 4 and Table S1). We conclude that the barrier for CO oxidation is considerably lower on the finite systems than on the rod-model.

3.3 SnO_X Regeneration via Molecular O_2 Dissociation

To maintain a catalytic cycle, the SnO_x-phases should be regenerated by O_2 adsorption and dissociation. O_2 adsorbs on $Pt(111)/Pt_3Sn$ with an adsorption energy of −0.90 eV in a fcc-Pt position (Fig. 3a). The O–O distance is in this state elongated from 1.23 Å in gas phase to 1.41 Å. The transition state for dissociation occurs with an O–O distance of 1.83 Å and a barrier of 0.27 eV (Fig. 3a). The O_2 dissociation is, thus, only weakly activated on the Pt-skin which is in agreement with previous reports for Pt(111) [38]. The barrier calculated with respect to O_2 in the gas phase is −0.64 eV.

At low temperature, the catalyst is expected to be CO poisoned, with only a limited number of empty sites available for O_2 dissociation on the metal phase. Therefore, O_2 dissociation is here investigated at the (SnO_2)/Pt interface of the different SnO_X models in their **C state requiring only one empty metal site, rather than two metal sites.

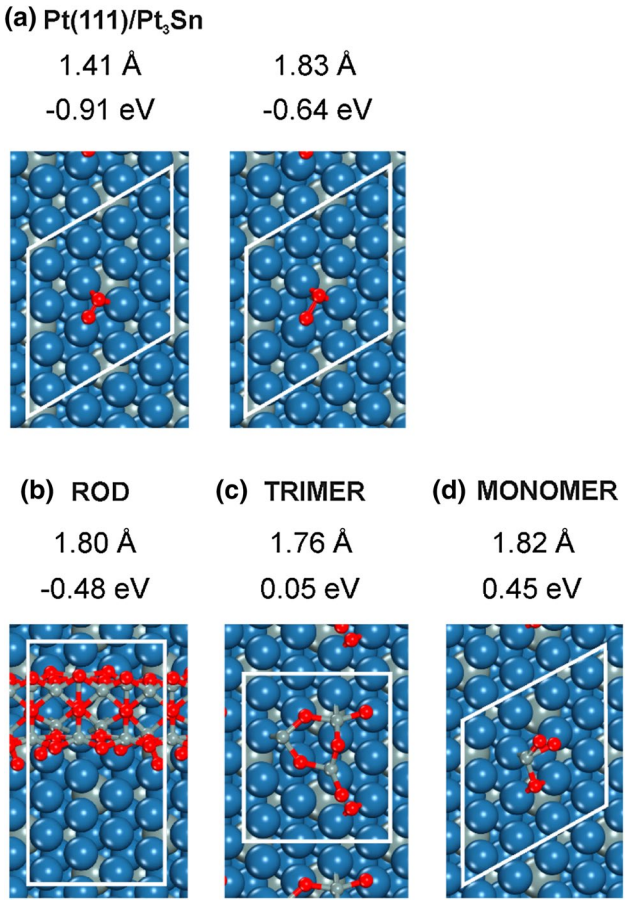

Fig. 3 **a** Structural models of the reactant and transition state for O_2 dissociation reaction on Pt-skin. **b–d** Structural models of the O_2 transition state at the considered SnO_X/Pt-skin systems. The O–O distance of the dissociating bond is given together with the reaction barriers (with respect to O_2 in gas phase). Atomic color codes: O (red), Sn (gray) and Pt (blue)

Transition states are shown in Fig. 3. At the transition state, the dissociating O–O bond is about 1.80 Å for all model systems. The barrier with respect to O_2 in the gas phase increases considerably from the rod-model to the finite systems; − 0.48 eV (rod), 0.05 eV (trimer), 0.45 eV (monomer), see Fig. 3b-d. The interface O_2 dissociation barrier at the state *** of the monomer (one Sn ad atom) is 0.14 eV with respect to O_2 in gas phase, which is much higher than a transition state neighboring the Sn ad atom which has an activation energy of − 0.47 eV with respect to gas phase O_2, see ESM. In case of the rod model, there are many possibilities to regenerate the rod. One example is oxygen transfer reactions in the rod at state **C; interface oxygen atoms can be created by transport of the O-vacancies to the top of the rod, making them accessible for O_2 regeneration. From this example, it is obvious that the rod-model, in contrast to the finite systems, does not require metal sites for O_2 dissociation reactions.

We close this section by noting that there might be a possibility to adsorb O_2 at the monomer and trimer, if an O_2 is adsorbed in an on top configuration, requiring only one metal site. The adsorption energy is in this case − 0.29 eV for the trimer and − 0.02 eV for the monomer. The corresponding dissociation energies (with respect to the adsorbed states) are 0.34 eV and 0.47 eV for the trimer and monomer, respectively.

Possible catalytic cycles for CO oxidation over the investigated systems are summarized in Fig. 4. For the rod-system, the CO oxidation reactions proceed with barriers of 1.01 and 1.20 eV, respectively. The corresponding barriers are lower for the monomer and the trimer. Even if the monomer model is regenerated to an SnO_3 state, the CO oxidation proceeds easily for ABC to A*C. The barrier for oxygen regeneration is, instead, higher for the finite systems as compared to the rod. In a previous microkinetic model of CO oxidation at metal supported rod-model [24], it was found that the O_2 dissociation became slightly rate controlling, about 15%, at 400 K. Because the finite SnO_2-models have larger O_2 dissociation barriers, they will likely have a higher rate control at similar temperatures.

4 Conclusions

This work emphasizes interface effects during CO oxidation on Pt-alloys nanoparticles taking place at the SnO_2/Pt_3Sn interface. When the Pt phase is CO poisoned, the SnO_2/Pt_3Sn interface enables a pathway for low temperature CO oxidation. Dependent on the degree of segregation, different interface effects can be anticipated and here we have investigated monomeric, trimeric and periodic $(SnO_2)_X$-rod models. Regardless of the size of the studied $(SnO_2)_X$-phase, CO oxidation can proceed with low barriers, which explain the experimentally observed low temperature activity. The reoxidation with O_2 is, however, more activated for the monomer and the trimer than on the rod-model, potentially forming a bottleneck for low temperature CO oxidation on the finite SnO_X-units. Summarizing, the co-catalytic role of an SnO_X/Pt_3Sn interface will manifest itself in a low temperature activity provided that the SnO_X-phase can be regenerated with oxygen.

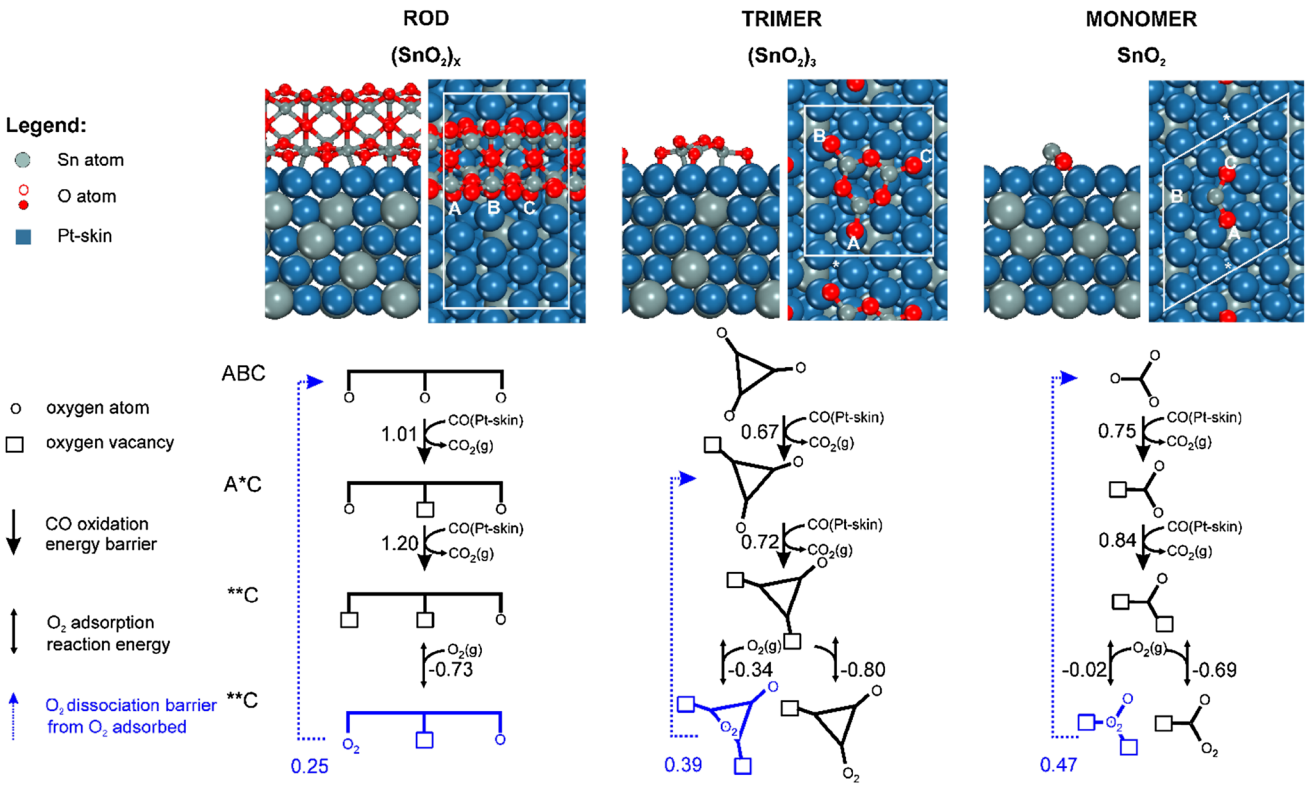

Fig. 4 Schematic representation of putative catalytic cycles of CO oxidation for the considered systems. The O_2 dissociation barriers are here given with respect to adsorbed O_2

Acknowledgements Financial support from the Swedish Research Council (2016-05234) and Chalmers Area of Advance Transport is acknowledged. The Competence Centre for Catalysis (KCK) is hosted by Chalmers University of Technology and is financially supported by the Swedish Energy Agency and the member companies: AB Volvo, ECAPS AB, Haldor Topsøe A/S, Scania CV AB, Volvo Car Corporation AB, and Wärtsila Finland Oy. The calculations were performed at C3SE (Göteborg) and Uppmax (Uppsala) via a SNIC grant.

References

1. Moscu A, Veyre L, Thieuleux C, Meunier F, Schuurman Y (2015) CO PROX over Pt-Sn/Al_2O_3: a combined kinetic and in situ DRIFTS study. Catal Today 258:241–246. https://doi.org/10.1016/j.cattod.2014.12.036
2. Moscu A, Schuurman Y, Veyre L, Thieuleux C, Meunier F (2014) Direct evidence by in situ IR CO monitoring of the formation and the surface segregation of a Pt-Sn alloy. Chem Commun 50(62):8590–8592. https://doi.org/10.1039/c4cc03208j
3. Michalak WD, Krier JM, Alayoglu S, Shin JY, An K, Komvopoulos K, Liu Z, Somorjai GA (2014) CO oxidation on PtSn nanoparticle catalysts occurs at the interface of Pt and Sn oxide domains formed under reaction conditions. J Catal 312:17–25. https://doi.org/10.1016/j.jcat.2014.01.005
4. Schubert MM, Kahlich MJ, Feldmeyer G, Huttner M, Hackenberg S, Gasteiger HA, Behm RJ (2001) Bimetallic PtSn catalyst for selective CO oxidation in H_2-rich gases at low temperatures. Phys Chem Chem Phys 3(6):1123–1131. https://doi.org/10.1039/b008062o
5. Lam YL, Criado J, Boudart M (1977) Enhancement by inactive gold of rate of H_2–O_2 reaction on active palladium—ligand effect. Nouveau Journal De Chimie-New J Chem 1 (6):461–466
6. Liu P, Norskov JK (2001) Ligand and ensemble effects in adsorption on alloy surfaces. Phys Chem Chem Phys 3(17):3814–3818. https://doi.org/10.1039/b103525h
7. Strasser P, Koh S, Anniyev T, Greeley J, More K, Yu CF, Liu ZC, Kaya S, Nordlund D, Ogasawara H, Toney MF, Nilsson A (2010) Lattice-strain control of the activity in dealloyed core-shell fuel cell catalysts. Nat Chem 2(6):454–460. https://doi.org/10.1038/nchem.623
8. Escudero-Escribano M, Malacrida P, Hansen MH, Vej-Hansen UG, Velazquez-Palenzuela A, Tripkovic V, Schiotz J, Rossmeisl J, Stephens IEL, Chorkendorff I (2016) Tuning the activity of Pt alloy electrocatalysts by means of the lanthanide contraction. Science 352(6281):73–76. https://doi.org/10.1126/science.aad8892
9. Ferrando R, Jellinek J, Johnston RL (2008) Nanoalloys: from theory to applications of alloy clusters and nanoparticles. Chem Rev 108(3):845–910. https://doi.org/10.1021/cr040090g

10. Gilroy KD, Ruditskiy A, Peng HC, Qin D, Xia YN (2016) Bimetallic nanocrystals: syntheses, properties, and applications. Chem Rev 116(18):10414–10472. https://doi.org/10.1021/acs.chemrev.6b00211
11. Roldan Cuenya B, Behafarid F (2015) Nanocatalysis: size- and shape-dependent chemisorption and catalytic reactivity. Surf Sci Rep 70(2):135–187. https://doi.org/10.1016/j.surfrep.2015.01.001
12. Kozlov SM, Kovacs G, Ferrando R, Neyman KM (2015) How to determine accurate chemical ordering in several nanometer large bimetallic crystallites from electronic structure calculations. Chem Sci 6(7):3868–3880. https://doi.org/10.1039/C4SC03321C
13. Neitzel A, Kovács G, Lykhach Y, Kozlov SM, Tsud N, Skála T, Vorokhta M, Matolín V, Neyman KM, Libuda J (2016) Atomic ordering and Sn segregation in Pt–Sn nanoalloys supported on CeO_2 thin films. Top Catal. https://doi.org/10.1007/s11244-016-0709-5
14. Tao F, Grass ME, Zhang YW, Butcher DR, Renzas JR, Liu Z, Chung JY, Mun BS, Salmeron M, Somorjai GA (2008) Reaction-driven restructuring of Rh-Pd and Pt-Pd core-shell nanoparticles. Science 322(5903):932–934. https://doi.org/10.1126/science.1164170
15. Fernandes VR, Van den Bossche M, Knudsen J, Farstad MH, Gustafson J, Venvik HJ, Gronbeck H, Borg A (2016) Reversed hysteresis during CO oxidation over Pd75Ag25(100). ACS Catal 6(7):4154–4161. https://doi.org/10.1021/acscatal.6b00658
16. Zheng J, Busch M, Artiglia L, Skála T, Rossmeisl J, Agnoli S (2016) A DFT structural investigation of new bimetallic PtSnx surface alloys formed on the Pt(110) surface and their interaction with carbon monoxide. J Phys Chem C 120(44):25306–25316. https://doi.org/10.1021/acs.jpcc.6b06638
17. Kim HY, Henkelman G (2013) CO oxidation at the interface of Au nanoclusters and the stepped-CeO_2(111) surface by the Mars–van Krevelen mechanism. J Phys Chem Lett 4(1):216–221. https://doi.org/10.1021/jz301778b
18. Radmilovic V, Richardson TJ, Chen SJ, Ross PN Jr (2005) Carbon-supported Pt–Sn electrocatalysts for the anodic oxidation of H_2, CO, and H_2/CO mixtures. Part I. Microstructural characterization. J Catal 232(1):199–209. https://doi.org/10.1016/j.jcat.2005.03.007
19. Jugnet Y, Loffreda D, Dupont C, Delbecq F, Ehret E, Aires F, Mun BS, Akgul FA, Liu Z (2012) Promoter effect of early stage grown surface oxides: a near-ambient-pressure XPS study of CO oxidation on PtSn bimetallics. J Phys Chem Lett 3(24):3707–3714. https://doi.org/10.1021/jz301802g
20. Fu Q, Li W-X, Yao Y, Liu H, Su H-Y, Ma D, Gu X-K, Chen L, Wang Z, Zhang H, Wang B, Bao X (2010) Interface-confined ferrous centers for catalytic oxidation. Science 328(5982):1141–1144. https://doi.org/10.1126/science.1188267
21. Pan Q, Weng X, Chen M, Giordano L, Pacchioni G, Noguera C, Goniakowski J, Shaikhutdinov S, Freund H-J (2015) Enhanced CO oxidation on the oxide/metal interface: from ultra-high vacuum to near-atmospheric pressures. ChemCatChem 7(17):2620–2627. https://doi.org/10.1002/cctc.201500394
22. Kudernatsch W, Peng G, Zeuthen H, Bai Y, Merte LR, Lammich L, Besenbacher F, Mavrikakis M, Wendt S (2015) Direct visualization of catalytically active sites at the FeO–Pt(111) interface. ACS Nano 9(8):7804–7814. https://doi.org/10.1021/acsnano.5b02339
23. Lin J, Wang X, Zhang T (2016) Recent progress in CO oxidation over Pt-group-metal catalysts at low temperatures. Chin J Catal 37(11):1805–1813. https://doi.org/10.1016/S1872-2067(16)62513-5
24. Vandichel M, Moscu A, Gronbeck H (2017) Catalysis at the rim: a mechanism for low temperature CO oxidation over Pt_3Sn. ACS Catal 7(11):7431–7441. https://doi.org/10.1021/acscatal.7b02094
25. Ma DD, Ding D, Huang JJ, Zhang H, Zheng YP, Chen MS, Wan HL (2017) Promoting effect of bismuth oxide on palladium for low-temperature carbon monoxide oxidation. ChemCatChem 9(3):499–504. https://doi.org/10.1002/cctc.201601181
26. Rodriguez JA, Grinter DC, Liu ZY, Palomino RM, Senanayake SD (2017) Ceria-based model catalysts: fundamental studies on the importance of the metal-ceria interface in CO oxidation, the water-gas shift, CO_2 hydrogenation, and methane and alcohol reforming. Chem Soc Rev 46(7):1824–1841. https://doi.org/10.1039/c6cs00863a
27. Perdew JP, Burke K, Ernzerhof M (1996) Generalized gradient approximation made simple. Phys Rev Lett 77(18):3865–3868
28. Kresse G, Furthmuller J (1996) Efficiency of ab-initio total energy calculations for metals and semiconductors using a plane-wave basis set. Comput Mater Sci 6(1):15–50. https://doi.org/10.1016/0927-0256(96)00008-0
29. Kresse G, Furthmuller J (1996) Efficient iterative schemes for ab initio total-energy calculations using a plane-wave basis set. Phys Rev B 54(16):11169–11186. https://doi.org/10.1103/PhysRevB.54.11169
30. Blochl PE (1994) Projector augmented-wave method. Phys Rev B 50(24):17953–17979. https://doi.org/10.1103/PhysRevB.50.17953
31. Pack JD, Monkhorst HJ (1977) Special points for Brillouin-zone integrations—a reply. Phys Rev B 16(4):1748–1749
32. Monkhorst HJ, Pack JD (1976) Special points for Brillouin-zone integrations. Phys Rev B 13(12):5188–5192
33. Mills G, Jonsson H, Schenter GK (1995) Reversible work transition-state theory - application to dissociative adsorption of hydrogen. Surf Sci 324(2–3):305–337. https://doi.org/10.1016/0039-6028(94)00731-4
34. Henkelman G, Jónsson H (2000) Improved tangent estimate in the nudged elastic band method for finding minimum energy paths and saddle points. J Chem Phys 113(22):9978–9985. https://doi.org/10.1063/1.1323224 doi
35. Henkelman G, Jónsson H (1999) A dimer method for finding saddle points on high dimensional potential surfaces using only first derivatives. J Chem Phys 111(15):7010–7022. https://doi.org/10.1063/1.480097 doi
36. Mulheran PA, Harding JH (1992) The stability of SnO_2 surfaces. Model Simul Mater Sci Eng 1(1):39
37. Batzill M, Diebold U (2005) The surface and materials science of tin oxide. Prog Surf Sci 79(2–4):47–154. https://doi.org/10.1016/j.progsurf.2005.09.002
38. Eichler A, Mittendorfer F, Hafner J (2000) Precursor-mediated adsorption of oxygen on the (111) surfaces of platinum-group metals. Phys Rev B 62(7):4744–4755. https://doi.org/10.1103/PhysRevB.62.4744